

**Nature of antiferromagnetic order in epitaxially strained multiferroic SrMnO<sub>3</sub> thin films**L. Maurel,<sup>1,2,3</sup> N. Marcano,<sup>2,4</sup> T. Prokscha,<sup>5</sup> E. Langenberg,<sup>1,6</sup> J. Blasco,<sup>2,3</sup> R. Guzmán,<sup>7</sup> A. Suter,<sup>5</sup> C. Magén,<sup>3,7,8</sup>  
L. Morellón,<sup>1,3</sup> M. R. Ibarra,<sup>1,3</sup> J. A. Pardo,<sup>1,7,9</sup> and P. A. Algarabel<sup>2,3,\*</sup><sup>1</sup>*Instituto de Nanociencia de Aragón, Universidad de Zaragoza, C/ Mariano Esquillor s/n, 50018 Zaragoza, Spain*<sup>2</sup>*Instituto de Ciencia de Materiales de Aragón, CSIC-Universidad de Zaragoza, C/ Pedro Cerbuna 12, 50009 Zaragoza, Spain*<sup>3</sup>*Departamento de Física de la Materia Condensada, Universidad de Zaragoza, C/ Pedro Cerbuna 12, 50009 Zaragoza, Spain*<sup>4</sup>*Centro Universitario de la Defensa, Academia General Militar, Crta. Huesca s/n, 50090 Zaragoza, Spain*<sup>5</sup>*Laboratory for Muon Spin Spectroscopy, Paul Scherrer Institute-CH-5232 Villigen PSI, Switzerland*<sup>6</sup>*Centro de Investigación en Química Biológica y Materiales Moleculares, Universidad de Santiago de Compostela, C/ Jenaro de la Fuente s/n, 15782 Santiago de Compostela, Spain*<sup>7</sup>*Laboratorio de Microscopías Avanzadas, Instituto de Nanociencia de Aragón, Universidad de Zaragoza, C/ Mariano Esquillor s/n, 50018 Zaragoza, Spain*<sup>8</sup>*Fundación ARAID, C/ María de Luna 11, planta 1ª, Edificio CEEI Aragón, 50018 Zaragoza, Spain*<sup>9</sup>*Departamento de Ciencia y Tecnología de Materiales y Fluidos, Universidad de Zaragoza, C/ María de Luna 3, 50018 Zaragoza, Spain*

(Received 8 May 2015; revised manuscript received 24 June 2015; published 17 July 2015)

Epitaxial films of SrMnO<sub>3</sub> and bilayers of SrMnO<sub>3</sub>/La<sub>0.67</sub>Sr<sub>0.33</sub>MnO<sub>3</sub> have been deposited by pulsed laser deposition on different substrates, namely, LaAlO<sub>3</sub> (001), (LaAlO<sub>3</sub>)<sub>0.3</sub>(Sr<sub>2</sub>AlTaO<sub>6</sub>)<sub>0.7</sub> (001), and SrTiO<sub>3</sub> (001), allowing us to perform an exhaustive study of the dependence of antiferromagnetic order and exchange bias field on epitaxial strain. The Néel temperatures ( $T_N$ ) of the SrMnO<sub>3</sub> films have been determined by low-energy muon spin spectroscopy. In agreement with theoretical predictions,  $T_N$  is reduced as the epitaxial strain increases. From the comparison with first-principles calculations, a crossover from G-type to C-type antiferromagnetic orders is proposed at a critical tensile strain of around  $1.6 \pm 0.1\%$ . The exchange bias (coercive) field, obtained for the bilayers, increases (decreases) by increasing the epitaxial strain in the SrMnO<sub>3</sub> layer, following an exponential dependence with temperature. Our experimental results can be explained by the existence of a spin-glass (SG) state at the interface between the SrMnO<sub>3</sub> and La<sub>0.67</sub>Sr<sub>0.33</sub>MnO<sub>3</sub> films. This SG state is due to the competition between the different exchange interactions present in the bilayer and favored by increasing the strain in the SrMnO<sub>3</sub> layer.

DOI: [10.1103/PhysRevB.92.024419](https://doi.org/10.1103/PhysRevB.92.024419)

PACS number(s): 75.70.-i, 75.75.-c, 76.75.+i

**I. INTRODUCTION**

Multiferroic materials showing simultaneous magnetic and ferroelectric ordering have become the subject of intensive research in recent years [1–4]. The coexistence of both phenomena in a single-phase material is rare because the classical mechanisms for ferroelectricity and magnetism are in most cases independent or even mutually excluding [5]. The so-called “ $d^0$ -ness” rule in ferroelectric perovskites, where the hybridization takes place between occupied O ( $2p$ ) orbitals and empty ( $3d$ ) orbitals of the transition-metal cation, makes challenging the search for magnetoelectric multiferroics showing efficient coupling between ferromagnetic and ferroelectric orders, even more at room temperature. These materials would allow the use of electric fields to control or even switch magnetization, and conversely magnetic fields to act on the electric polarization, thus enabling a range of potentially disruptive magnetoelectric applications like electric-writing magnetic-reading random access memories, electrically tunable spintronic and microwave devices, and room-temperature-operation high-sensitivity magnetic sensors [6].

Recent theoretical results predicted that some  $ABO_3$  perovskite oxides, showing no electric or magnetic ordering in the bulk, could become multiferroic when the unit cell volume is increased, as a result of a strong interaction between the

spin ordering and the lattice phonons (so-called “spin-phonon coupling”) [7]. One of the possible mechanisms for that is the epitaxial strain, which was previously used to induce ferroelectricity in SrTiO<sub>3</sub> [8], induce a ferromagnetic to antiferromagnetic phase transition in SrCoO<sub>3</sub> [9], or turn CaMnO<sub>3</sub> into an incipient ferroelectric [10]. The accomplishment of strain-engineered multiferroism in tensile-strained epitaxial EuTiO<sub>3</sub> films [11], which become ferroelectric below 250 K and ferromagnetic below 4 K [12], was a major advancement in the field that opened a radically novel approach for reaching room-temperature magnetoelectric effects, specially suited to integrated technologies. However, magnetoelectric coupling in this perovskite oxide is fundamentally limited by magnetism and ferroelectricity originating from different lattice sites; namely, from Eu<sup>2+</sup> at the  $A$  site and off-centered Ti<sup>4+</sup> at the  $B$  site, respectively [7]. Next challenge is then both to raise the magnetic and ferroelectric ordering temperatures and to increase the magnetoelectric coupling to be able, in the future, to use these materials to design functional devices at room temperature.

Alkaline-earth manganese perovskites are particularly promising for strain engineering of multiferroism [13,14]. The spontaneous polarization is expected to be driven by the off-centering of the Mn<sup>4+</sup> ion, with  $d^3$  electronic configuration and net magnetic moment; consequently, strong coupling of ferroelectric and magnetic orderings could be expected. First experimental indications that this approach might be feasible have been recently given; ferroelectricity was demonstrated for Ba-substituted SrMnO<sub>3</sub> single crystals (in which chemical

\*algarabe@unizar.es

pressure was applied by partial substitution of Ba for Sr [15], and incipient ferroelectricity appeared in highly strained epitaxial  $\text{CaMnO}_3$  films [10]. In the case of antiferromagnetic (AFM)  $\text{SrMnO}_3$  (SMO) a first-principles study predicted strain-induced ferroelectricity [16]. Actually, the emergence of a polar state in epitaxial films of SMO grown under a tensile strain of 1.7% was experimentally demonstrated by second harmonic generation (SHG) measurements [17].

The crystal structure of bulk SMO in thermodynamic equilibrium is hexagonal ( $\alpha$ -SMO) below 1700 K, and cubic ( $\beta$ -SMO) above this temperature [18]. The cubic perovskite phase can be kept in a metastable state at 300 K [19], and has a lattice parameter of 3.805 Å [20]. Unstrained cubic SMO shows G-type AFM ordering with  $2.6 \pm 0.2 \mu_B$  magnetic moment per  $\text{Mn}^{4+}$  atom below its Néel temperature ( $T_N$ ) [21,22], which was reported between 233 and 260 K [20–23], this dispersion being probably caused by the variable oxygen stoichiometry in the samples [22]. Further studies showed how the magnetic ordering strongly depends on the tetragonality ( $c/a$  ratio) of the unit cell [16,22,24]. Discrepancies were found on several reports, finding, in all cases, changes in the antiferromagnetic ordering but at different values of the  $c/a$  ratio. This work is focused on the study of  $T_N$  in strained thin films, where it has been predicted not only a change of the AFM order but a decrease of  $T_N$  upon epitaxial strain [16], concomitant with the development of a polar state [14].

To check the validity of the theoretical predictions, in this paper, we report on a comprehensive investigation of the AFM order of SMO epitaxial thin films grown on different substrates, thus with different degrees of epitaxial strain. The experimental study of AFM ordering in thin films is challenging due to the large diamagnetic signal of the substrate in comparison to the film. We have overcome this problem by determining Néel temperatures of the different films by means of low-energy muon spectroscopy (LE- $\mu$ SR). This technique was successfully used before to determine the ordering temperature in AFM thin films such as  $\text{La}_{2-x}\text{Sr}_x\text{CuO}_4$  [25],  $\text{TbMnO}_3$  [26], and  $\text{Pr}_{0.5}\text{Ca}_{0.5}\text{MnO}_3$  [27]. Using our results obtained in the case of SMO and the theoretical calculations extracted from the literature [16], a temperature-strain magnetic phase diagram is proposed.

One possibility to give functionality to the AFM polar state of SMO films is its coupling with a ferromagnetic (FM) film at the interface through the exchange bias effect. To explore this scenario, the  $\text{La}_{0.67}\text{Sr}_{0.33}\text{MnO}_3$  (LSMO) system was selected as the FM layer because of its structural similarity to SMO. By doping  $\text{SrMnO}_3$  with La, the system becomes FM in the range of 20%–40% La content in bulk, but magnetic properties of manganites not only depend on La doping but on strain as well [28,29]. Coupling the FM and AFM order of both materials by means of exchange bias effect would open the door to the control of the magnetic properties applying an electric field in multiferroic heterostructures [30]. We report the dependence of this phenomenon on the epitaxial strain and temperature in SMO/LSMO bilayers.

## II. EXPERIMENTAL DETAILS

SMO films were grown by pulsed laser deposition (PLD) with a KrF laser at a substrate temperature of 850 °C using

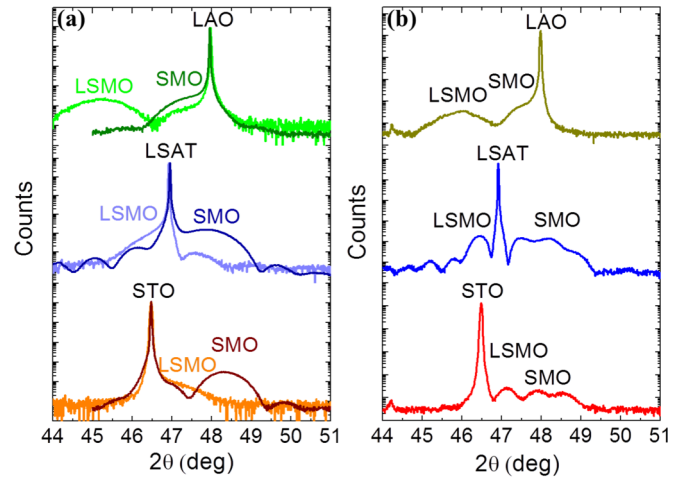


FIG. 1. (Color online) XRD patterns around the symmetric 002 reflection for the SMO and LSMO layers (a) and SMO/LSMO bilayers (b) grown on LAO, LSAT, and STO substrates.

an oxygen pressure of 100 mTorr and a laser fluence of  $1 \text{ J/cm}^2$ . (001)-oriented single-crystal substrates of  $\text{LaAlO}_3$  (LAO),  $(\text{LaAlO}_3)_{0.3}(\text{Sr}_2\text{AlTaO}_6)_{0.7}$  (LSAT), and  $\text{SrTiO}_3$  (STO) were used to induce nominal epitaxial strain values of  $-0.40\%$ ,  $1.67\%$ , and  $2.60\%$ , respectively. In the case of LSMO layers, the growth was carried out at 400 mTorr  $\text{O}_2$  pressure, a substrate temperature of 800 °C and a laser fluence of  $0.8 \text{ J/cm}^2$ . The same substrates induce in this case nominal strains of  $-2.07\%$  (LAO),  $0.03\%$  (LSAT), and  $0.88\%$  (STO). In all the cases, the films were annealed at 1 bar of oxygen and 800 °C during 30 minutes.

The films thickness was determined by means of x-ray reflectivity (XRR) measurements and fits were performed by the LEPTOS software (Bruker AXS) obtaining also the average density of the strained materials [31]. To study the crystal quality of the films, x-ray diffraction (XRD) measurements were carried out. First of all, samples of LSMO and SMO were grown separately on every substrate to study their individual properties. Symmetric  $\theta/2\theta$  scans around the 002 substrate peak were performed to measure the out-of-plane lattice parameter of the films [Fig. 1(a)] obtaining, in the case of SMO, values of 3.855 Å for the films grown on LAO, 3.775 Å on LSAT, and 3.756 Å on STO. For the LSMO films, the values obtained were 4.006 Å on LAO, 3.912 Å on LSAT, and 3.833 Å on STO. All these values are in accordance with previous works [32]. Values lower than 0.03 degrees for the full width at half maximum (FWHM) of the rocking curves around the symmetric peaks evidenced a high crystalline quality in all cases. Reciprocal space maps (RSM) along the 103 asymmetric reflection (in pseudocubic axes for the case of LSMO) were performed to certify that films are fully strained (not shown).

LE- $\mu$ SR experiments were performed using the low-energy muon spectrometer at the Paul Scherrer Institute (PSI), Switzerland [33–35]. The muon energy is tunable in the range of 0.5–30 keV, thus allowing muon implantation in thin films at specific depths. Monte Carlo simulations were performed to determine the implantation depth [36,37]. The measurements were performed in the temperature range 5–300 K. For muon

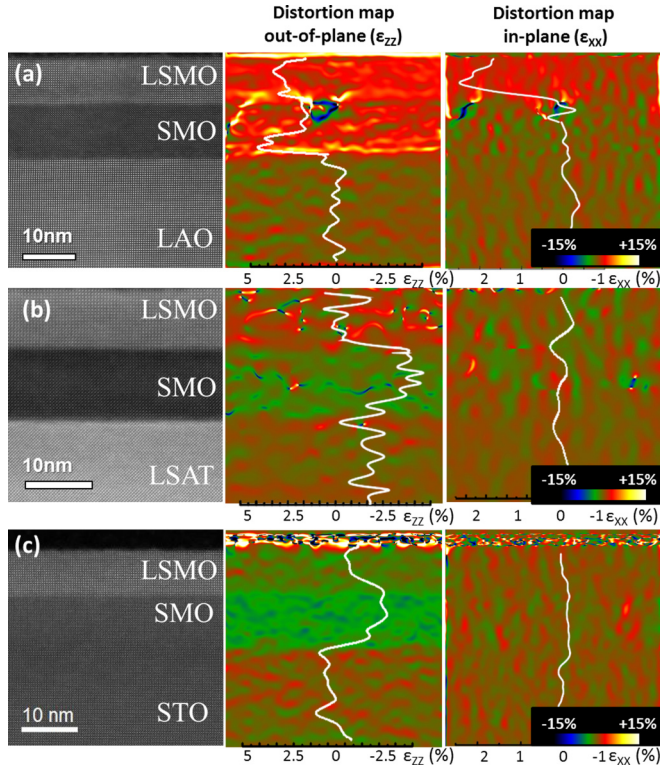


FIG. 2. (Color online) STEM and GPA results for the SMO/LSMO bilayers grown on LAO (a), LSAT (b), and STO (c). Left panels correspond to the HAADF-STEM images of the region under study. Central and right panels represent out-of-plane and in-plane distortion maps for the samples, respectively. The white line shows the averaged distortion profile (see text for details).

experiments, 10-nm-thick SMO films were grown on the three selected substrates. A bulk sample of cubic  $\text{SrMnO}_{2.97}$  was synthesized according to Tichy *et al.* [38] and used as a test sample to determine the Néel temperature of unstrained SMO.

For the exchange bias study, SMO (8 nm)/LSMO (8 nm) bilayers were grown by PLD on LAO, LSAT, and STO substrates. XRD measurements around the substrate 002 peak [Fig. 1(b)] show a diffraction pattern built up from the interference of two patterns corresponding to different unit cells (of different materials) and their respective von Laue oscillations (indicating the high crystal quality of both films).

High angle annular dark field (HAADF) scanning transmission electron microscopy (STEM) was performed in a probe corrected FEI Titan to probe locally the crystal quality of our films. As illustrated in Fig. 2, an abrupt interface between the different layers is obtained in all the cases as well as high quality of the films along the full thickness. Strain maps have been determined from the STEM images by the geometrical phase analysis (GPA) [40] and are shown in Fig. 2 for the bilayers deposited on the three substrates. Out-of-plane and in-plane distortion maps are shown in the central and right panels, respectively. The in-plane distortion  $\varepsilon_{xx}$ , defined by the in-plane film ( $a_{\text{film}}$ ) and substrate ( $a_{\text{subs}}$ ) lattice parameters as

$$\varepsilon_{xx} = \frac{a_{\text{film}} - a_{\text{subs}}}{a_{\text{subs}}} \quad (1)$$

is zero for the bilayers grown on LSAT and STO [Figs. 2(b) and 2(c)], indicating that both SMO and LSMO are fully

strained. In the case of the bilayer deposited on LAO [Fig. 2(a)],  $\varepsilon_{xx}$  is zero for the SMO but  $\varepsilon_{xx} \approx 2\%$  for the LSMO pointing out that the SMO is fully strained but the LSMO is partially relaxed, being the in-plane lattice closer to the bulk value. The formation of misfit dislocations appears to be the relaxation mechanism, as evidenced by the singularities observed at the SMO/LSMO interface in Fig. 2(a). The out-of-plane distortion map  $\varepsilon_{zz}$ , defined by the out-of-plane film ( $c_{\text{film}}$ ) and substrate ( $c_{\text{subs}}$ ) lattice parameters as

$$\varepsilon_{zz} = \frac{c_{\text{film}} - c_{\text{subs}}}{c_{\text{subs}}} \quad (2)$$

is shown in the central panel for the three bilayers. The average values estimated from the GPA are in good agreement with the ones obtained from XRD measurements.

Macroscopic magnetic properties of the SMO/LSMO bilayers were measured by a superconducting quantum interference device (SQUID, Quantum Design) magnetometer. The applied magnetic field was always parallel to the film plane and along the [100] direction of the substrate. The field-cooled (FC) and zero-field-cooled (ZFC) magnetization measurements were made on heating from 5 to 400 K, after the sample was cooled from 300 K down to the selected temperature with and without the magnetic field, respectively. The isothermal hysteresis loops were measured after FC from 300 K under 5000-Oe applied magnetic field.

### III. RESULTS AND DISCUSSION

#### A. Low-energy muon spectroscopy: temperature-strain magnetic phase diagram

In  $\mu\text{SR}$  experiments, positive muons with  $\sim 100\%$  spin polarization are implanted into the sample, where they stop at interstitial sites within a few picoseconds without noticeable loss of polarization. Due to the interactions of the muon spins with internal local magnetic fields  $B_l$ , the magnetic moments of the muons precess with the Larmor frequency  $\omega_L = 2\pi\nu = \gamma_\mu B_l$  ( $\gamma_\mu = 2\pi \times 135.5 \text{ MHz/T}$  is the muons gyromagnetic ratio) until they decay with a lifetime  $\tau_\mu = 2.2 \mu\text{s}$  emitting a positron and two undetected neutrinos. The positron is emitted preferentially along the muon spin direction at the time of the decay. The detection of the positron emission rate in counters aligned along the initial muon spin direction allows one to monitor the decay rate of the muon spin polarization along its initial spin direction. The positron emission rate  $dN/dt$  is given by

$$\frac{dN}{dt} = N_{\text{bkg}} + \frac{N_0}{\tau_\mu} e^{-t/\tau_\mu} [1 \pm AG(t)], \quad (3)$$

where  $N_{\text{bkg}}$  is a time-independent background signal,  $N_0$  is a normalization factor,  $A$  is the average asymmetry of the decay angular distribution (typically 0.2–0.3), and  $G(t)$  describes the decay rate of the muon spin polarization. The + or – signs are appropriate for positron counters in the direction of, or opposite to, the muon spin, respectively.

In  $\mu\text{SR}$  experiments with bulk materials, muons with energy of  $\sim 4.1 \text{ MeV}$  are used. In this case, the mean stopping depth in condensed matter is  $\sim 100 \mu\text{m}$ . In the case of thin films, LE- $\mu\text{SR}$  uses epithermal muons ( $\sim 15 \text{ eV}$ ), which are created by moderating surface muons. After reacceleration,

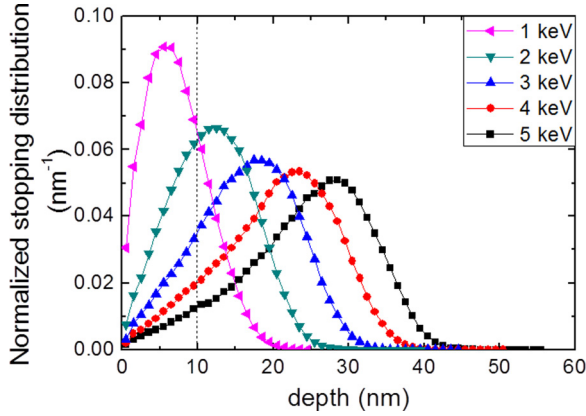


FIG. 3. (Color online) The normalized stopping distribution of muons with different implantation energies (values given in the inset) of a 10-nm-thick SMO film deposited on a single-crystal STO substrate calculated using TRIM.SP [36,37]. The lines are a guide for the eye. The dashed line denotes the position of the interface of the sample with STO substrate.

applying a voltage to the sample controls the final muon implantation energy. By tuning the implantation energy between 1 and 30 keV, mean depths between 10 nm and few hundred nanometers can be chosen. Figure 3 displays the normalized stopping distribution of muons in a SMO film deposited on a STO substrate for different implantation energies calculated using the Monte Carlo simulation program TRIM.SP [36,37]. This Monte Carlo simulation shows that the lowest muon implantation energy ( $E_{\text{impl}} = 1$  keV) yields a mean implantation depth of about 5 nm and approximately 80% of the muons stopped at the SMO film, which is optimal for the study of the 10-nm SMO films taking into account the density of the material determined by XRR measurements.

Substrates of  $1/2'' \times 1/2''$  in the case of LSAT and LAO and  $10 \times 10$  mm<sup>2</sup> in the case of STO were glued onto a nickel-coated aluminum plate with silver paint. In addition, an SMO bulk sample was measured as a reference for the  $T_N$  of the unstrained material. In this case, a higher implantation energy was used ( $E_{\text{impl}} = 11$  keV) in order to increase the signal-to-noise ratio.

The experiments were performed in ultrahigh vacuum at a pressure of  $10^{-9}$  mbar. To reach temperatures in the range of 4 to 300 K, a continuous-flow cryostat KONTI was used. LE- $\mu$ SR measurements were performed in a weak transverse magnetic field (wTF) of 10 mT applied perpendicular to the initial muon spin polarization and to the film surface in order to obtain the value of  $T_N$ .

In a weak transverse field  $B_{\text{ext}}$ , the data are fit with the relaxation function  $G(t) = G_x(t)$ :

$$G_x(t) = f_T^{\text{TF}} \cos(\gamma_\mu B_l t + \phi) e^{-\lambda_T t} + f_L^{\text{TF}} e^{-\lambda_L t}, \quad (4)$$

which designates the paramagnetic part of the muon-spin polarization.  $f_T^{\text{TF}}$  and  $f_L^{\text{TF}}$  reflect the fraction of the muons having their spin initially transverse and longitudinal to the local magnetic field direction, respectively.

The first term describes the muon precession with frequency  $\omega_\mu = \gamma_\mu B_l$  in the local magnetic field  $B_l$  at the muon stopping site, where in our case  $B_l = B_{\text{ext}}$  above and below  $T_N$ .  $\Phi$

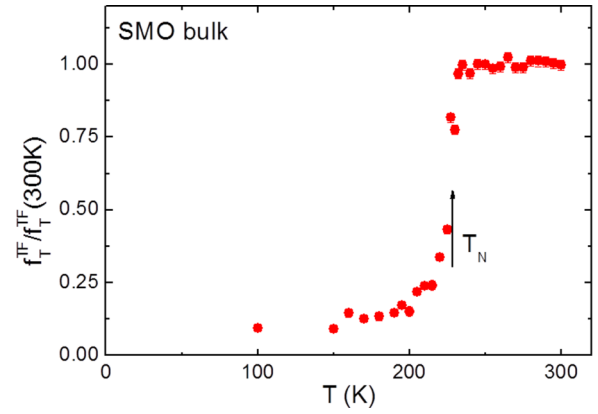


FIG. 4. (Color online) The transverse  $f_T^{\text{TF}}$  fraction as a function of temperature determined in an external transverse magnetic field of 10 mT for  $E_{\text{impl}} = 11$  keV, normalized to the fraction at 300 K for bulk SMO. The arrow shows the bulk magnetic ordering temperature  $T_N = 227$  K.

is a phase offset due to the spin rotation of the implanted muons relative to the positron detectors. The relaxation rate  $\lambda_T$  describes how fast this precession is depolarized by a distribution or fluctuations of magnetic fields (relaxation by static and dynamic effects). The second term represents the part of nonprecessing muon spins. Relaxation can appear here in the presence of fluctuating magnetic fields (relaxation only by dynamics).

Above  $T_N$ ,  $f_T^{\text{TF}}$  is at its maximum, since only the external magnetic field is present inside the sample, and  $\lambda_T \sim 0.06 \mu\text{s}^{-1}$ , caused by weak nuclear dipolar fields. Note that  $f_L$  is not zero here, but represents the background fraction of muons missing the sample and stopping in the Ni backing of the sample holder (40%–50% of all muons, depending on the sample size), where about 1/3 of the muons experience a longitudinal magnetic field, much larger than  $B_{\text{ext}}$  due to the ferromagnetism present in the Ni coating. For these muons  $\lambda_L < 0.01 \mu\text{s}^{-1}$ ;  $f_T^{\text{TF}} = 0$  for muons stopping in Ni due to the large internal magnetic fields causing a very fast depolarization of muons having their spins transverse to the internal field [39]. Below  $T_N$ , the internal magnetic fields inside the sample superimpose on the weak external magnetic field, leading to a strong dephasing of the precession signal. This produces a decrease of  $f_T^{\text{TF}}$  to a level corresponding to the nonmagnetic volume fraction of the sample. Note that for the 10-nm-thin samples, about 20% of the muons are stopping in the nonmagnetic substrates (see Fig. 3), where they experience only the weak external magnetic field. We find the same value for the internal field as above  $T_N$ , i.e.,  $B_l = B_{\text{ext}}$ , whereas the depolarization rate  $\lambda_T$  increases by a factor 2–3 at low temperatures ( $< 100$  K), which we attribute to the presence of static stray fields in nonmagnetic volumes of the SMO films, originating from the antiferromagnetic volumes nearby. A decrease in  $f_T^{\text{TF}}$  with a simultaneous increase in  $f_L^{\text{TF}}$  probes static magnetism.

Figure 4 shows the transverse fraction  $f_T^{\text{TF}}$  as a function of the temperature for the bulk SrMnO<sub>2.97</sub> reference sample. The data are normalized to the values in the paramagnetic regime at 300 K. The magnetic transition temperature  $T_N$  was defined after the maximum at the derivative of the transverse fraction data  $f_T^{\text{TF}}/f_T^{\text{TF}}(300 \text{ K})$  (T). This yields a transition temperature

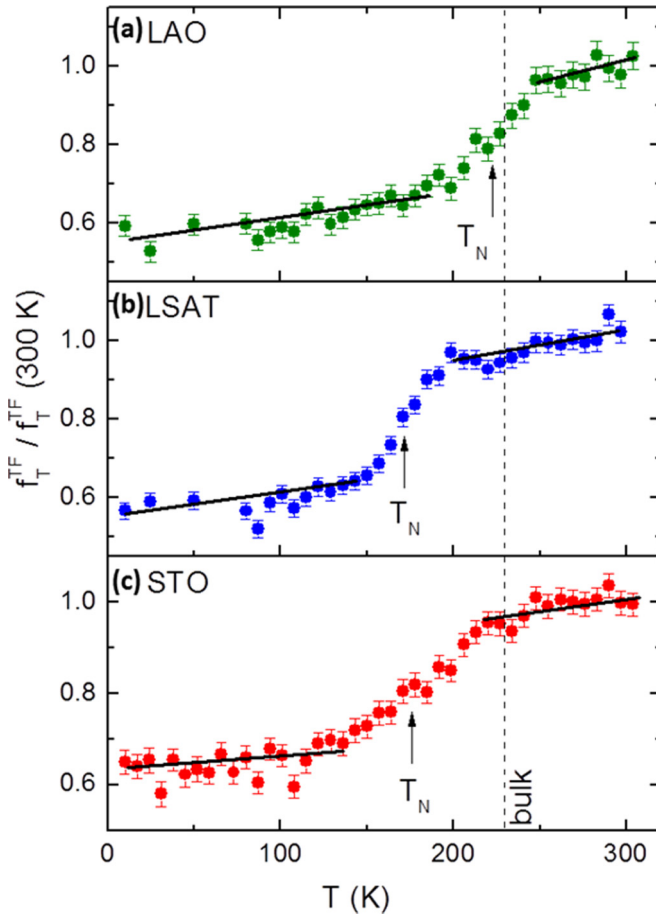


FIG. 5. (Color online) The transverse  $f_T^{TF}$  fraction as a function of temperature determined in an external transverse magnetic field of 10 mT for  $E_{\text{impl}} = 1$  keV, normalized to the fraction at 300 K for 10-nm-thick SMO film on LAO (a), LSAT (b), and STO (c). The dashed line denotes the bulk magnetic ordering temperature obtained from the present wTF  $\mu$ SR measurements and the arrows the Néel Temperatures determined at the maximum slope.

value  $T_N = 227(1)$  K, which is close to the reported values of  $T_N$  for the bulk sample (from 233 to 260 K depending on authors [20–23]).

Figure 5 shows transverse fraction  $f_T^{TF}$  as a function of the temperature for the 10-nm-thick SMO films on LAO, LSAT, and STO. The data are normalized to the values at 300 K. Contrary to the bulk material, the thin films do not exhibit a sharp transition at  $T_N$  but a broad decay in temperature. Such a broad decay in the transverse fraction can be associated to a distribution of transition temperatures due to the existence of ordered oxygen vacancies in the films [17]. These vacancies would modify the superexchange paths yielding local changes in  $T_N$ . According to this scenario,  $T_N$  is obtained by fitting the derivative curve of the data with a Gaussian curve and taking its center as  $T_N$  (Stilp *et al.*) [25]. The corresponding values for the magnetic transition temperature  $T_N$  are listed in Table I. The results show that  $T_N$  decreases as tensile stress increases.

The values of  $T_N$  determined from wTF LE- $\mu$ SR measurements (red dots) and the predicted dependence obtained by Lee *et al.* [16] (black dots and black continuous line) are shown in Fig. 6. The experimental  $T_N$  decreases with increasing

TABLE I. Values of  $T_N$  obtained from weak transverse field LE- $\mu$ SR data for the 10-nm-thick SMO films with different strains and the bulk SMO sample used as a reference.

| Sample                | Strain (%) | $T_N$ (K) |
|-----------------------|------------|-----------|
| LAO//SMO              | -0.4       | 224 (8)   |
| Bulk                  | 0          | 227 (1)   |
| NGO//SMO <sup>a</sup> | 1.4        | 196       |
| LSAT//SMO             | 1.7        | 171 (4)   |
| STO//SMO              | 2.6        | 180 (13)  |

<sup>a</sup>Obtained from Nakao *et al.* [41].

the epitaxial strain, that is in qualitative agreement with the predictions [16]. In a direct comparison, the experimental value of  $T_N$  obtained for the bulk sample does not fit with the predicted value for the unstrained SMO [16]. For this reason, we propose a model where the predicted tendency is shifted + 17 K to fit the bulk experimental value. With our proposed model, the Néel temperatures for the films grown on LAO and LSAT follow qualitatively the theoretical prediction. Moreover, the theoretical model predicts a crossover in the AFM order from G to C type at an epitaxial strain of 2%. After this change,  $T_N$  remains almost constant. In order to explain the experimental Néel temperature obtained for the STO//SMO film, we propose that the transition between G and C antiferromagnetic orders takes place at an epitaxial strain of around  $1.6 \pm 0.1\%$  (see shadow region for our proposed model and black dashed line for the theoretical predictions [16] in Fig. 6), slightly lower than the theoretically predicted of 2%. As predicted by the model,  $T_N$  remains almost constant for strains slightly above this value. It is noteworthy that other criterion to obtain  $T_N$  [27] would yield a different value for the transition temperature and this would shift the  $T_N$  in Fig. 6. However, those values would follow qualitatively the theoretical prediction.

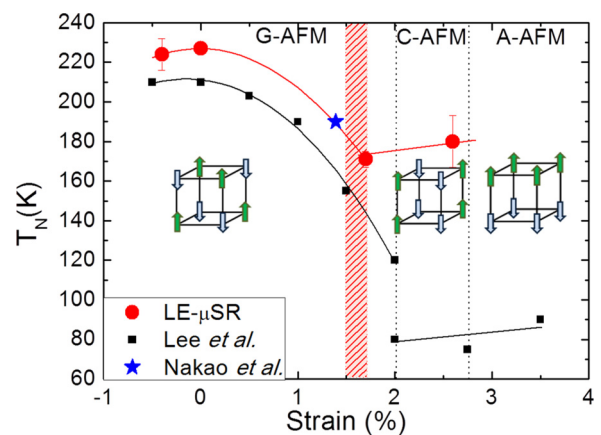


FIG. 6. (Color online) Values of  $T_N$  for SMO thin films as a function of the strain as inferred from LE- $\mu$ SR experiments (red dots). Black dots (and black continuous line) represent the theoretical predictions from Lee *et al.* [16]. The red line denotes our proposed model, and the blue star represents  $T_N$  of SMO on NGO obtained by Nakao *et al.* [41]. Dotted black line represents the threshold value between different AFM ordering determined by Lee *et al.* [16], and shadow red area our proposed model.

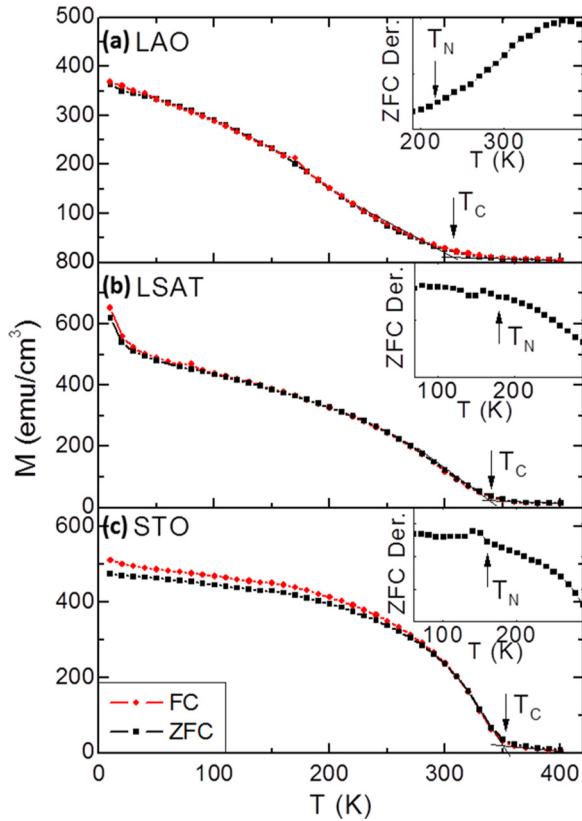


FIG. 7. (Color online) ZFC and 1 kOe FC magnetization curves measured during warming at 5 kOe for the bilayers grown on LAO (a), LSAT (b), and STO (c). ZFC derivative is plotted in the insets. Measured  $T_N$  by LE- $\mu$ SR and obtained  $T_C$  are indicated by arrows.

The proposed dependence of  $T_N$  on strain is further supported from previous neutron diffraction experiments performed on epitaxial SMO thin films grown on NdGaO<sub>3</sub> (NGO), with a lattice parameter close but smaller than LSAT, obtaining a G-type AFM order and a Néel temperature of 190 K [41]. NGO is orthorhombic and induces strain levels of 1.28% and 1.52% along the a and b axis on the SMO film. Considering an average strain of 1.4%, the AFM type order and the value of  $T_N$  obtained from neutron experiments (blue star in Fig. 6) is in good agreement with our proposed phase diagram. Summarizing, we have determined the Néel temperatures of SMO films under different epitaxial strains, and a temperature-strain magnetic phase diagram is proposed. Our experimental results support the theoretical prediction of a decrease of  $T_N$  with increasing strain and a change of the AFM order from G to C type at a critical strain of  $1.6 \pm 0.1\%$ .

### B. Exchange bias in SMO/LSMO bilayers

As a first step, we have characterized the magnetic properties of the FM LSMO layer in the bilayers under study. The contribution of the SMO layer to the overall magnetization of the bilayer is negligible at the magnetic fields applied in this work due to its AFM character. The magnetization curves as a function of temperature, measured while warming up at an applied magnetic field of 5 kOe after zero-field cooling and 1 kOe field cooling, are shown in Fig. 7 for the bilayers

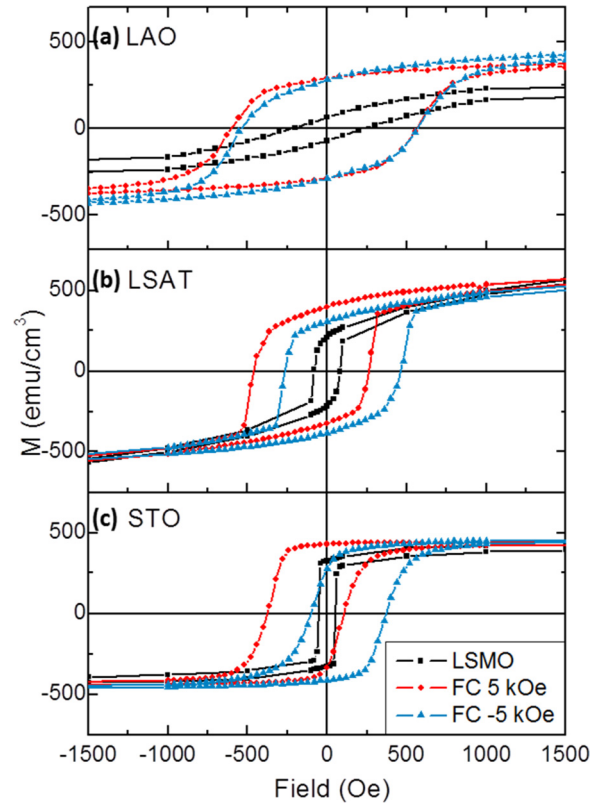


FIG. 8. (Color online) Isothermal hysteresis loops at 5 K for the monolayers of LSMO on the different substrates (black squares). The same for the SMO/LSMO bilayers after cooling down in presence of a magnetic field of 5 kOe (red dots) and  $-5$  kOe (blue triangles).

grown on the three substrates. The Curie temperatures ( $T_C$ ) obtained are  $308 \pm 5$ ,  $334 \pm 5$ , and  $348 \pm 3$  K for the samples deposited on LAO, LSAT, and STO, respectively (the value corresponding to the bulk material is  $T_C = 370$  K [42]). The dependence of  $T_C$  on the epitaxial strain induced by the substrate ( $-2.07\%$  on LAO,  $0.03\%$  on LSAT, and  $0.88\%$  on STO) is in good agreement with the model proposed by Millis *et al.* [43] and the experimental values obtained by Adamo *et al.* [32]. It is worth mentioning that the increase in the magnetization observed at low temperatures for the film grown on LSAT [Fig. 7(b)] is due to the contribution of paramagnetic impurities present in the bare substrates. The derivatives of the ZFC measurements are presented in the inset of Fig. 7. For the films grown on LSAT and STO weak anomalies appear at  $T \approx 175$  K and can be associated to ordering temperatures of the SMO layer, in good agreement with our previous LE- $\mu$ SR experiments. For the film grown on LAO, the possible anomaly is hidden by a higher slope of the curve at the expected  $T_N$ .

The isothermal low-temperature hysteresis loops measured under ZFC of LSMO monolayers with the magnetic field applied along the [100] axis for the three substrates studied in this work are presented in Fig. 8. The hysteresis loops have been measured from  $-50$  to  $+50$  kOe, but for clarity only the data between  $-1.5$  and  $1.5$  kOe are shown. For the film grown on the LAO substrate, our measurement clearly shows the presence of perpendicular magnetic anisotropy at low temperature and a saturation magnetization (at 50 kOe)

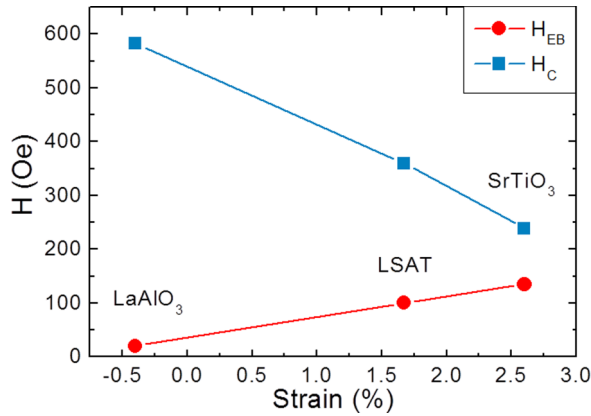


FIG. 9. (Color online) Values of  $H_{EB}$  (red dots) and  $H_C$  (blue squares) fields obtained from Fig. 8 as a function of the epitaxial strain induced by different substrates.

$\approx 320$  emu/cm<sup>3</sup> much lower than the value observed in bulk LSMO [42]. In the case of our LSMO films grown on LSAT and STO, they show in plane magnetic anisotropy, and a saturation magnetization value (at fields higher than 20 kOe) of  $534 \pm 5$  emu/cm<sup>3</sup>, corresponding to a value of  $3.29 \pm 0.03 \mu_B/\text{f.u.}$  (per formula unit), in agreement with the spin-only theoretical value  $3.33 \mu_B/\text{f.u.}$  and the experimental bulk LSMO magnetization [42]. Such a dependence of both the magnetic anisotropy and saturation magnetization on strain is in full agreement with previous works [28].

We also present in Fig. 8, at the same magnetic field range, the hysteresis loops of the SMO/LSMO bilayers measured after cooling down at an applied magnetic field of 5 kOe. An evident change of the magnetic anisotropy takes place for the SMO/LSMO bilayer with respect to the LSMO single film grown on LAO. In the case of the bilayer, the magnetic anisotropy is easy plane and the saturation magnetization is  $532 \pm 5$  emu/cm<sup>3</sup> corresponding to  $3.29 \pm 0.03 \mu_B/\text{f.u.}$ , equal to the value obtained in the LSMO single films grown on LSAT and STO. This change in the magnetic properties observed in SMO/LSMO bilayers is related to the partial relaxation of the epitaxial strain observed in the XRD measurements and reflected in the change of the out-of-plane lattice parameter from 4.008 Å, in the single layer, to 3.945 Å, for the bilayer, (Fig. 1) and corroborated by GPA in-plane strain analysis where it is shown that the LSMO film is relaxed [Fig. 2(a)]. This strain effect is also observed in the value of  $T_C$  obtained in our LAO//SMO/LSMO bilayer ( $T_C \approx 308$  K), higher than the previously reported value in LAO/LSMO single layer of  $\approx 280$  K [32].

Analyzing the results obtained at 5 K (Fig. 8), an increase of the coercive field in all the samples was observed as well as a shift in the magnetic loop opposite to the applied magnetic field. This behavior corresponds to the typical exchange bias effect occurring in hysteresis loops of FM/AFM bilayers that are exchange coupled after field cooling below the Néel temperature of the AFM layer [44,45].

This shift in the coercive field strongly depends on the strain of the films (Fig. 9). The exchange bias field is defined as  $H_{EB} = |H_+ + H_-|/2$ , where  $H_+$  and  $H_-$  denote the right and left coercive fields, respectively.  $H_{EB}$  increases as the strain

on the SMO layer increases, changing from 20 Oe for a strain of  $-0.40\%$  (LAO) to 135 Oe for 2.61% (STO). Furthermore, the enhancement of the coercive field, defined as  $H_C = |H_+ - H_-|/2$ , observed in the SMO/LSMO bilayers compared to the single LSMO layers agrees with the existence of a FM-AFM exchange coupling. In Fig. 9, we can observe that  $H_C$  decreases as the strain on the SMO layer increases. This behavior can be associated to the well-known dependence of the coercive field on strain through a stress-induced anisotropy [28,46].

In the case of G-type or C-type AFM orders of the SMO layer proposed from our LE- $\mu$ SR experiments, no pinning effects of the FM LSMO layer is expected due to spin compensated structure of the SMO monolayers. Therefore, the exchange bias effect observed must be associated to a decompensation on the spin structure at the SMO/LSMO interface. The exchange bias effect in LSMO/SMO bilayers and LSMO/SMO/LSMO trilayers, deposited on (001)-oriented STO substrates, has been deeply studied by Ding *et al.* [47] and Jungbauer *et al.* [48], respectively. In both cases, the existence of exchange bias effect has been explained by assuming the existence of a spin-glass (SG) state at the interface between the LSMO and SMO layers. The origin of the interfacial SG state is associated to the competition between the AFM superexchange interaction in the SMO layer and the FM double-exchange interaction in the LSMO layer through the interfacial exchange coupling [47].

This scenario is supported in our work by the observed exponential dependence of thermal variation of  $H_{EB}$  and  $H_C$  for the three bilayers studied (see Fig. 10). Such a behavior is considered as a fingerprint that the origin of the  $H_{EB}$  and  $H_C$  is due to the existence of spin frustration, and has been previously reported not only in LSMO/SMO bilayers [47] and LSMO/SMO/LSMO trilayers [48], but also in other systems, such as Ni/Ni<sub>76</sub>Mn<sub>24</sub> [49], La<sub>1-x</sub>Ca<sub>x</sub>MnO<sub>3</sub> FM ( $x = 0.33$ )/AFM (0.67) multilayers [50] and Co/CuMn bilayers [51]. In Fig. 10, we show the fits for the temperature dependence of  $H_{EB}$  and  $H_C$  performed in our SMO/LSMO bilayers grown on LAO, LSAT, and STO using the phenomenological formulas

$$H_{EB} = H_{EB}^0 e^{-T/T_1} \quad \text{and} \quad H_C = H_C^0 e^{-T/T_2}, \quad (5)$$

where  $H_{EB}^0$  and  $H_C^0$  are the extrapolation of  $H_{EB}$  and  $H_C$  at zero temperature;  $T_1$  and  $T_2$  are constants. In all the cases,  $H_{EB}$  vanishes at around 100 K being this temperature much lower than the Néel temperature of SMO determined by LE- $\mu$ SR spectroscopy and associated with the existence of a blocking temperature above which the AFM order of SMO cannot maintain an unidirectional anisotropy [47].

The presence of an interfacial SG state can also explain the observed increase of  $H_{EB}$  as the strain on the SMO layer increases. From the magnetic hysteresis loops shown in Fig. 8, we observe that the magnetization is not depressed in the SMO/LSMO bilayer compared with the corresponding LSMO film. At the same time, these results indicate that the SG state takes place, at least mainly, in the SMO layer, being the magnetization of the LSMO layer almost undisturbed in the bilayers. By increasing the lattice parameter of the substrate, the strain on the SMO layer increases,  $T_N$  decreases and a reduction of the AFM super-exchange interaction takes place. In the opposite side, by increasing the substrate lattice

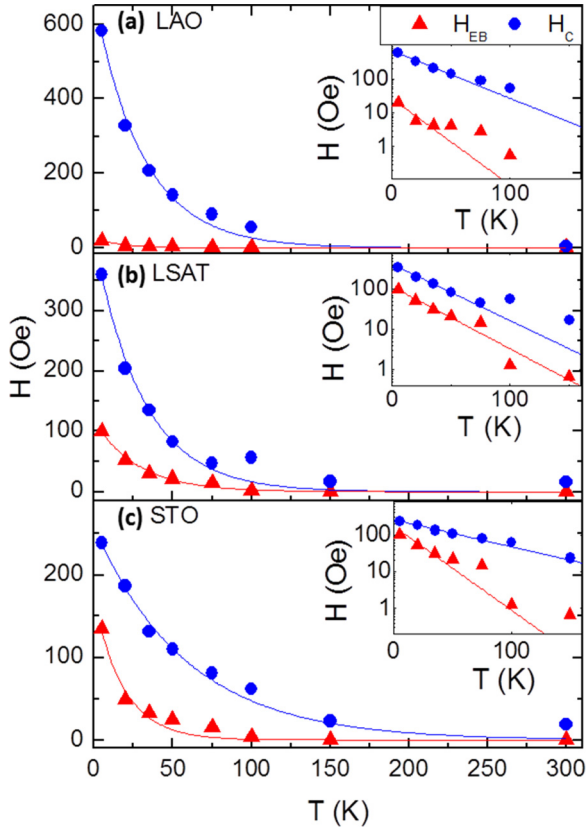


FIG. 10. (Color online) Thermal dependence of  $H_{EB}$  and  $H_C$  fields [obtained from isothermal hysteresis loops as a function of temperature (not shown)] of the bilayers grown on LAO (a), LSAT (b), and STO (c) after cooling down the sample from 300 K to the selected temperature in a magnetic field of 5 kOe. The solid lines are fits to the exponential temperature dependencies for SG behavior shown in Eq. (5). The insets show both, the temperature dependence of  $H_{EB}$  and  $H_C$  and the obtained fits in logarithmic scale (see text for details).

parameter,  $T_C$  of LSMO increases producing an increase of the FM double-exchange interaction. Assuming that the SG state is associated to the competition between the AFM super-exchange interaction in the SMO layer and the FM double-exchange interaction in the LSMO layer through the interfacial exchange coupling, an increase of the substrate lattice parameter favors the existence of the interfacial SG state in the SMO layer as the AFM superexchange interaction is decreased and the FM double-exchange interaction is increased disturbing the AFM order of the SMO layer at the interface.

An exhaustive study of the exchange bias effect using SG has demonstrated that  $H_{EB}$  increases by increasing the SG layer thickness [51]. We suggest that a similar behavior takes place in our films: by increasing the substrate lattice parameter, the SG state is favored by the competition between the different exchange interactions and therefore, the thickness of the SG layer ( $t_{SG}$ ) is increasing, being  $t_{SG,LAO} < t_{SG,LSAT} < t_{SG,STO}$  and consequently,  $H_{EB,LAO} < H_{EB,LSAT} < H_{EB,STO}$ . This idea is in good agreement with our  $M(T)$  curves (see Fig. 7). For the bilayers deposited on LAO and LSAT, the ZFC and FC branches are equal within the experimental error. The bilayer deposited on STO shows a clear irreversibility between the

ZFC and FC curves indicating a thicker SG layer respect to the previous one. The existence of a SG layer at the interface of the SMO/LSMO bilayer can be also favored by the presence of oxygen vacancies. The cell volume of SMO films increases by increasing the strain. This fact can be related to the presence of oxygen vacancies which enlarge the out-of-plane lattice parameter since  $Mn^{3+}$  cation is larger than  $Mn^{4+}$ . The ordering of these vacancies at the interface [17,52,53] can act as local defects at the surface frustrating the magnetic interactions and inducing an SG effect on the material. Since oxygen vacancies are believed to further increase when strained [17,52], this effect should be enhanced as the lattice parameter of the substrate increases.

Although this model explains satisfactorily our experimental results, other possible explanations cannot be completely discarded. Other theoretical works propose that the exchange bias is driven by Dzyaloshinskii-Moriya exchange interactions at the ferroelectric perovskite interfaces [54]. Moreover, the possible existence of A-type AFM order in the SMO perovskite, under electron doping and tensile strain, has been also predicted theoretically [22,24] and would lead to a strong exchange bias effect. More studies and experiments, mainly at the interface are needed to elucidate the real magnetic structure at the SMO/LSMO interface.

#### IV. CONCLUSIONS

We have presented an exhaustive study of the magnetic properties of epitaxial SMO and SMO/LSMO bilayers deposited on different substrates under different strains. From wTF LE- $\mu$ SR spectroscopy, the dependence of the Néel temperature with the strain has been obtained and, by comparison with theoretical calculations, a temperature-strain magnetic phase diagram has been proposed. Our experimental results suggest the existence of a crossover between G-type and C-type AFM orders at a critical strain  $\approx 1.6 \pm 0.1\%$ . The dependence of  $H_{EB}$  with temperature and strain has been studied and explained assuming the existence of a SG state at the interface between the LSMO and SMO layers. The observed increase of  $H_{EB}$  with increasing strain in SMO films has been associated to an increase of the thickness of the SG layer due to the weakening of the AFM order in the SMO interface.

#### ACKNOWLEDGMENTS

This work was supported by the Spanish Ministerio de Economía y Competitividad through Project Nos. MAT2011-28532-C03-02, MAT2011-27553-C02, MAT2012-38213-C02-01, and MAT2014-51982-C2 including FEDER funding, by the Aragón Regional Government through projects E26 and CTPP4/11 and by the European Union under the Seventh Framework Programme under a contract for an Integrated Infrastructure Initiative Reference 312483-ESTEEM2. N. Marcano acknowledges the support of the Centro Universitario de la Defensa en Zaragoza (through Project 2013-03). We acknowledge the use of the microscopy infrastructure available in the Laboratorio de Microscopías Avanzadas (LMA) at Instituto de Nanociencia de Aragón (University of Zaragoza, Spain). Part of this work was performed at the Swiss Muon Source ( $S\mu S$ ), at the Paul Scherrer Institute (PSI, Switzerland).

- [1] N. A. Spaldin and M. Fiebig, *Science* **309**, 391 (2005).
- [2] W. Eerenstein, N. D. Mathur, and J. F. Scott, *Nature (London)* **442**, 759 (2006).
- [3] R. Ramesh and N. A. Spaldin, *Nat. Mater.* **6**, 21 (2007).
- [4] N. A. Spaldin, S. W. Cheong, and R. Ramesh, *Phys. Today* **63**, 38 (2010).
- [5] N. A. Hill, *J. Phys. Chem. B* **104**, 6694 (2000).
- [6] J. Ma, J. Hu, Z. Li, and C. W. Nan, *Adv. Mater.* **23**, 1062 (2011).
- [7] T. Birol, N. A. Benedek, H. Das, A. L. Wysocki, A. T. Mulder, B. M. Abbett, E. H. Smith, S. Ghosh, and C. J. Fennie, *Curr. Opin. Solid State Mater. Sci.* **16**, 227 (2012).
- [8] J. H. Haeni *et al.*, *Nature (London)* **430**, 758 (2004).
- [9] S. J. Callori, S. Hu, J. Bertinshaw, Z. J. Yue, S. Danilkin, X. L. Wang, V. Nagarajan, F. Klose, J. Seidel, and C. Ulrich, *Phys. Rev. B* **91**, 140405(R) (2015).
- [10] T. Günter, E. Bousquet, A. David, Ph. Boullay, Ph. Ghosez, W. Prellier, and M. Fiebig, *Phys. Rev. B* **85**, 214120 (2012).
- [11] C. J. Fennie and K. M. Rabe, *Phys. Rev. Lett.* **97**, 267602 (2006).
- [12] J. H. Lee *et al.*, *Nature (London)* **466**, 954 (2010).
- [13] J. Hong, A. Stroppa, J. Íñiguez, S. Picozzi, and D. Vanderbilt, *Phys. Rev. B* **85**, 054417 (2012).
- [14] S. Bhattacharjee, E. Bousquet, and P. Ghosez, *Phys. Rev. Lett.* **102**, 117602 (2009).
- [15] H. Sakai *et al.*, *Phys. Rev. Lett.* **107**, 137601 (2011).
- [16] J. H. Lee and K. M. Rabe, *Phys. Rev. Lett.* **104**, 207204 (2010).
- [17] C. Becher *et al.*, *Nat. Nanotechnol.* (2015).
- [18] V. F. Balakirev and Y. V. Golikov, *Inorg. Mater.* **42**, S49 (2006).
- [19] T. Negas and R. S. Roth, *J. Solid State Chem.* **1**, 409 (1970).
- [20] O. Chmaissem, B. Dabrowski, S. Kolesnik, J. Mais, D. E. Brown, R. Kruk, P. Prior, B. Pyles, and J. D. Jorgensen, *Phys. Rev. B* **64**, 134412 (2001).
- [21] T. Takeda and S. Ohara, *J. Phys. Soc. Jpn.* **37**, 275 (1974).
- [22] R. Søndena, P. Ravindran, S. Stolen, T. Grande, and M. Hanfland, *Phys. Rev. B* **74**, 144102 (2006).
- [23] K. Kikuchi, H. Chiba, M. Kikuchi, and Y. Syono, *J. Solid State Chem.* **146**, 1 (1999).
- [24] Z. Fang, I. V. Solov'yev, and K. Terakura, *Phys. Rev. Lett.* **84**, 3169 (2000).
- [25] E. Stilp, A. Suter, T. Prokscha, E. Morenzoni, H. Keller, B. M. Wojek, H. Luetkens, A. Gozar, G. Logvenov, and I. Božović, *Phys. Rev. B* **88**, 064419 (2013).
- [26] M. Bator, Y. Hu, H. Luetkens, C. Niedermayer, T. Prokscha, A. Suter, Z. Salman, M. Kenzelmann, C. H. Schneider, and T. Lippert, *Phys. Procedia* **30**, 137 (2012).
- [27] I. Komissarov, Y. Zhang, G. J. Nieuwenhuys, E. Morenzoni, T. Prokscha, A. Suter, and J. Aarts, *Europhys. Lett.* **83**, 47013 (2008).
- [28] F. Tsui, M. C. Smoak, T. K. Nath, and C. B. Eom, *Appl. Phys. Lett.* **76**, 2421 (2000).
- [29] L. Marin *et al.*, *Nano Lett.* **15**, 492 (2015).
- [30] C. A. F. Vaz, *J. Phys. Condens. Matter* **24**, 333201 (2012).
- [31] <https://www.bruker.com/products/x-ray-diffraction-and-elemental-analysis/x-ray-diffraction/xrd-software/overview/leptos.html>
- [32] C. Adamo *et al.*, *Appl. Phys. Lett.* **95**, 112504 (2009).
- [33] T. Prokscha, E. Morenzoni, K. Deiters, F. Foroughi, D. George, R. Kobler, A. Suter, and V. Vrankovic, *Nucl. Instrum. Methods Phys. Res., Sect. A* **595**, 317 (2008).
- [34] P. Bakule and E. Morenzoni, *Contemp. Phys.* **45**, 203 (2004).
- [35] E. Morenzoni, *Appl. Magn. Reson.* **13**, 219 (1997).
- [36] E. Morenzoni *et al.*, *Nucl. Instr. Meth. B* **192**, 254 (2002).
- [37] W. Eckstein, *Computer Simulation of Ion-Solid Interactions* (Springer, Berlin, Heidelberg, New York, 1991).
- [38] R. S. Tichy and J. B. Goodenough, *Solid State Sci.* **4**, 661 (2002).
- [39] H. Saadaoui *et al.*, *Phys. Procedia* **30**, 164 (2012).
- [40] M. J. Hÿtch, E. Snoeck, and R. Kilaas, *Ultramicroscopy* **74**, 131 (1998).
- [41] H. Nakao, H. Yamada, A. Sawa, K. Iwasa, J. Okamoto, T. Sudayama, Y. Yamasaki, and Y. Murakami, *Solid State Commun.* **185**, 18 (2014).
- [42] A. Urushibara, Y. Moritomo, T. Arima, A. Asamitsu, G. Kido, and Y. Tokura, *Phys. Rev. B* **51**, 14103 (1995).
- [43] A. J. Millis, T. Darling, and A. Migliori, *J. Appl. Phys.* **83**, 1588 (1998).
- [44] J. Nogués, J. Sort, V. Langlais, V. Skumryev, S. Suriñach, J. S. Muñoz, and M. D. Baró, *Phys. Rep.* **422**, 65 (2005).
- [45] J. Nogués and I. K. Schuller, *J. Magn. Magn. Mater.* **192**, 203 (1999).
- [46] S. Chikazumi, *Physics of Ferromagnetism* (Clarendon Press, Oxford, 1997).
- [47] J. F. Ding, O. I. Lebedev, S. Turner, Y. F. Tian, W. J. Hu, J. W. Seo, C. Panagopoulos, W. Prellier, G. Van Tendeloo, and T. Wu, *Phys. Rev. B* **87**, 054428 (2013).
- [48] M. Jungbauer, S. Hühn, M. Michelmann, E. Goering, and V. Moshnyaga, *J. Appl. Phys.* **113**, 17D709 (2013).
- [49] B. Aktas, Y. Öner, and H. Z. Durusoy, *J. Magn. Magn. Mater.* **119**, 339 (1993).
- [50] N. Moutis, C. Christides, I. Panagiotopoulos, and D. Niarchos, *Phys. Rev. B* **64**, 094429 (2001).
- [51] M. Ali, P. Adie, C. H. Marrows, D. Greig, B. J. Hickey, and R. L. Stamps, *Nat. Mater.* **6**, 70 (2007).
- [52] U. Aschauer, R. Pfenninger, S. M. Selbach, T. Grande, and N. A. Spaldin, *Phys. Rev. B* **88**, 054111 (2013).
- [53] F. Hou, T. Y. Cai, S. Ju, and M. R. Shen, *Appl. Phys. Lett.* **99**, 192510 (2011).
- [54] S. Dong, K. Yamauchi, S. Yunoki, R. Yu, S. Liang, A. Moreo, J. M. Liu, S. Picozzi, and E. Dagotto, *Phys. Rev. Lett.* **103**, 127201 (2009).